Dispersive Ground Plane Core–Shell Type Optical Monopole Antennas Fabricated with Electron Beam Induced Deposition

Hakkı Acar,* Toon Coenen, Albert Polman, and Laurens Kobus Kuipers

Center for Nanophotonics, FOM Institute, AMOLF Science Park 104, 1098 XG Amsterdam, The Netherlands

ABSTRACT

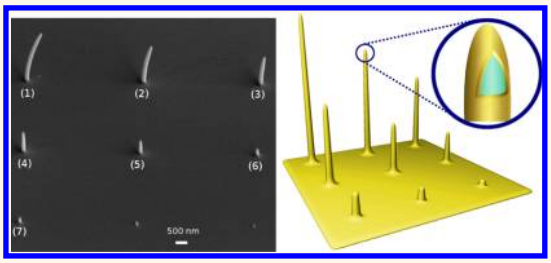

We present the bottom-up fabrication of dispersive silica core, gold cladding ground plane optical nanoantennas. The structures are made by a combination of electron-beam induced deposition of silica and sputtering of gold. The antenna lengths range from 300 to 2100 nm with size aspect ratios as large as 20. The angular emission patterns of the nanoantennas are measured with angle-resolved cathodoluminescence spectroscopy and compared with finite-element methods. Good overall correspondence between the the measured and calculated trends is observed. The dispersive nature of these plasmonic monopole antennas makes their radiation profile highly tunable.

KEYWORDS: core–shell nanoantenna · EBID · angle-resolved cathodoluminescence

Antennas have been indispensable tool of modern human civilization ever since the first radio communication in 1898.[1] They have been studied and engineered vigorously during the last 50 years in the radio frequency (RF) and microwave band of the electromagnetic spectrum. Research on their nanoscale optical counterparts has just been established in the past decade as parallel developments in nanotechnology.[2,3] The purpose of all antennas (conventional and optical) is the same, either to localize propagating electromagnetic radiation or to convert localized energy to electromagnetic radiation. In other words the antenna is the translational structure between free-space and a guiding device in order to transmit electromagnetic energy from the transmitting source to antenna or from the antenna to receiver.[4]

The combination of surface plasmon polaritons (SPP)—collective electron oscillations coupled to the external electromagnetic field—and nanoantennas makes it possible to squeeze the external electromagnetic field to dimensions much smaller than the diffraction limit. Reaching beyond the diffraction limit paves the way for novel single molecule microscopy[5,6] and spectroscopy,[7] near-field microscopy,[8] surface-enhanced Raman spectroscopy,[9] light harvesting for photovoltaics,[10,11] and light emission applications.[12]

The progress in nanostructuring techniques, such as electron beam lithography (EBL),[13,14] focused ion beam milling (FIB),[15,16] nanoimprint lithography (NIL),[17] makes it possible to fabricate and explore the nanoantennas with various geometry and dimension.[18–20] In addition to those commonly used top-down nanofabrication techniques, electron beam induced deposition (EBID), as a bottom up technique offers an alternative way for the fabrication of nanostructures down to 3 nm.[21] As a direct-write nanofabrication technique EBID allows fabrication of 3D structures without the need for resist. Despite its characteristic purity problem, being a direct fabrication technique with one-step process and possibility to build three-dimensional nanostructures, EBID is a promising technique for nanophotonic applications.

In this Letter we report a versatile and practical fabrication method for vertically oriented silica core–gold shell optical nanoantennas with aspect ratios as large as 20:1 (Figure 1). To characterize the optical properties of these nanoantennas, we study their 3D emission pattern with angle-resolved

* Address correspondence to acar@amolf.nl.

Received for review June 29, 2012 and accepted August 13, 2012.

Published online 10.1021/nn302907j

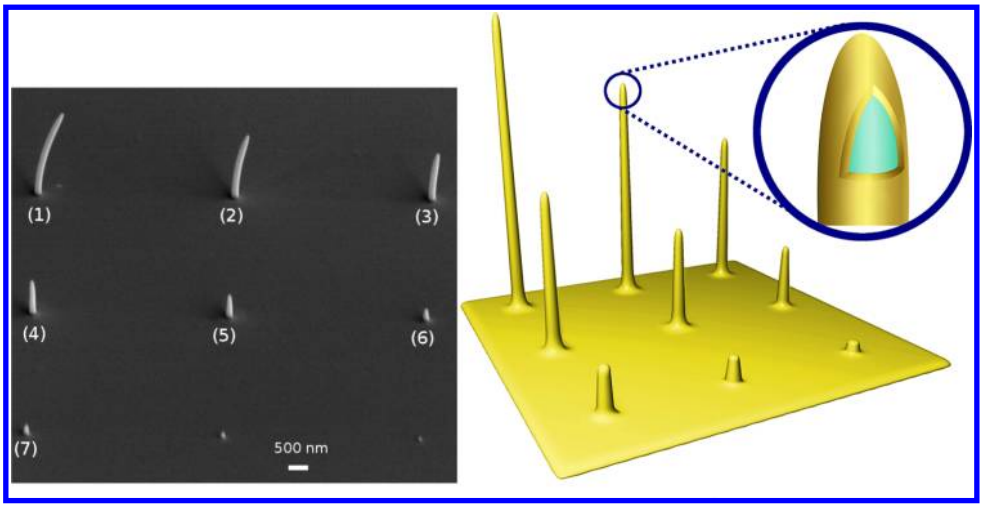

Figure 1. (a) SEM image of vertically oriented core−shell nanoantennas grown on a substrate composed of a 30 nm gold layer coated on top of a silicon wafer. The SEM micrograph is taken at an angle of 52°. The scale bar is 500 nm. (b) A schematic representation of the nanoantennas. The silica core is fabricated by EBID on the substrate, after which 30 nm gold is deposited, covering both the antenna and substrate.

cathodoluminescence (CL) microscopy.[22,23] The results are compared with finite-element simulations that model the excitation of the nanoantennas by using a point-like dipole on top of each antenna. Additionally, effective index mode calculations were performed in order to elucidate the plasmonic properties of the nanoantennas and the role of the core and shell thickness.

RESULTS AND DISCUSSION

The measured height of the antennas is given in Table 1: the tallest and shortest nanoantennas are 2100 and 200 nm, respectively. A slight tapering is observed for each antenna of which the angle varies between 1.80° and 7°; the larger the antennais, the smaller is the tapering. After the gold deposition onto the silica pillars three of the longest antennas developed a bend which we attribute to the strain induced by the thermal contraction mismatch between Au and SiO_2 during cooling after the Au sputtering process.

To study the optical properties of our nanoantennas we use CL microscopy. It is based on the coupling of a point dipole to the collective electron oscillations on the nanostructure. A point dipole is induced by the electrons from a focused beam of a scanning electron microscope (SEM), and the image charge of the incoming electron. The CL setup, incorporated into a FEI a XL-30 SFEG scanning electron microscope is composed of three parts: e-beam, a mirror, and CDD camera. First, inside the vacuum chamber there is a paraboloid aluminum mirror with 0.5 mm focal length and a hole on the focal point through which the electron beam can irradiate the sample (see Figure 2a). The light, emitted from the electron beam irradiated nanostructure (Figure 2b) is collected by the paraboloid mirror and directed onto a CCD array (Figure 2c). The paraboloid mirror is designed such that each pixel in the resulting image on the CCD array corresponds to a unique angle of emission from the structure. An optical filter is used to select only the wavelengths between 630 and 670 nm.

TABLE 1. Height of the Nanoantennas (nm)

rod no. 1	rod no. 2	rod no. 3	rod no. 4	rod no. 5	rod no. 6	rod no. 7
2100 ± 100	1550 ± 100	1200 ± 100	850 ± 100	550 ± 100	300 ± 50	200 ± 50

Figure 2d shows the emission pattern of the longest nanoantenna. This polar graph can be read in a way that the *z*-axis in Figure 2e passes through the dark spot at the center of the graph. The dark spot reflects the position of the hole in the paraboloid mirror through which the antenna is irradiated with the e-beam. The concentric circular patterns correspond to the angular emission as a function of ϕ and θ with θ and ϕ being mapped in the polar graph on r and ϕ, respectively: while the innermost ring in Figure 2d corresponds to the lobe emitted by the antenna with the smallest theta angle, the outermost ring corresponds to the lobe emitted with the highest theta angle, closest to the substrate surface (see Figure 2b). The color scale shows the number of photons collected per unit collection time, and the dark area toward the top is due to the aperture of the paraboloid mirror through which light is collected.

Our angle-resolved measurement is performed by irradiation of the top of the each nanoantenna by the focused electron beam. The electric dipole excites the SPP mode(s) along the nanoantenna and with CL microscopy we observe the out-coupling of this mode(s) to the far-field. Figure 3 panels a−g show the angle-resolved emission data of the individual antennas tabulated in Table 1 where the lengths of the nanoantennas vary from 2100 to 200 nm. This data is obtained by using a 650 nm bandpass filter with 40 nm bandwidth. The color scale in Figure 3 shows the photon count

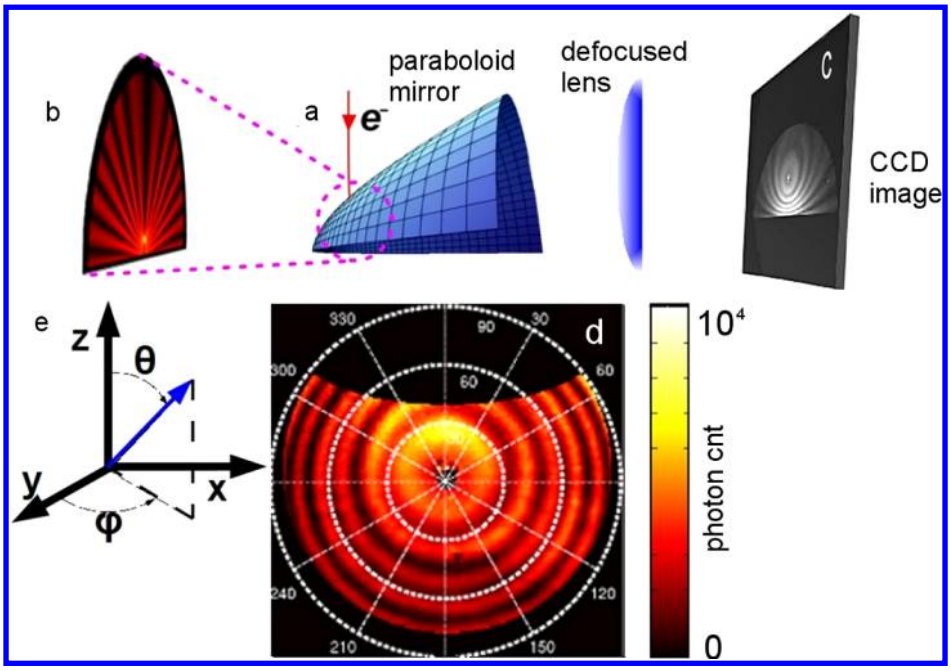

Figure 2. The angle-resolved CL setup: the sample at the focal point of the paraboloid mirror is irradiated by a focused electron beam of a SEM. The three-dimensional light emission is caused by the excited surface plasmons along the nanoantenna. The light is collected by a paraboloid mirror and sent to the CCD camera. The image with full wave vector information is converted to a polar graph where radial and angular coordinates correspond to azimuthal (ϕ: from 0° to 360°) and zenithal (θ: from 0° to 90°) spherical coordinates, respectively.

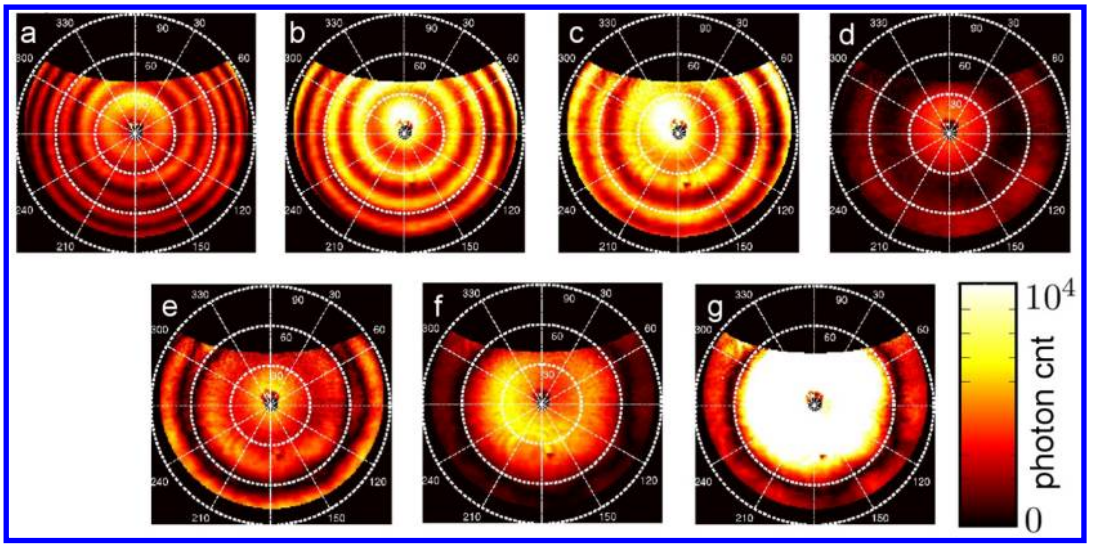

Figure 3. Measured angle-resolved emission patterns of nanoantennas at a wavelength of 650 nm. Each plot corresponds to the angle-resolved emission data of an individual antenna. From panels a−g the heights of the antennas are 2100, 1550, 1100, 800, 550, 300, and 200 nm, respectively. The circular emission patterns correspond to the lobes that antennas radiate upon irradiation by electron beam. The color scale corresponds to the photon counts between 0 and 10000. In each measurement photons are as collected for 3 min. The lack of data on top of each graph between 50° and 310° is caused by the parabolic mirror aperture.

collected from each of the seven nanoantennas. In Figure 3a we see that there are six circular patterns. We observe in Figure 3a−g that the number of lobes decreases with the decreasing height of the nanoantennas. The measured linear relation between the number of emitted lobes and the nanoantenna height is plotted in Figure 4

To better understand the optical properties of nanoantennas we also perform numerical calculations, using commercial finite-element modeling software[24] (COMSOL 4.2), to study the emission patterns of the nanoantennas. The geometry of the simulated nanoantennas is as follows: a silica core with 50 nm radius coaxially coated with gold cladding. The cap of the

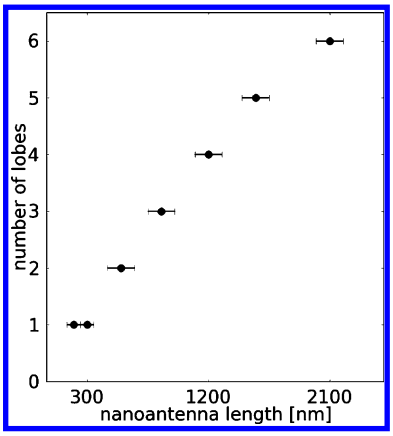

Figure 4. The measured relation between the length of the nanoantennas and the emitted number of lobes.

nanoantennas are designed as a hemisphere. Data from Palik et al.[25] is used for the optical constants of gold. The silica-shell nanoantennas are modeled on a gold substrate and the whole structure is inside a hemispherical simulation box with a radius of 20 μm. The hemisphere box is chosen because of its axial symmetry which is identical to the axial symmetry of the measured nanoantennas. Totally absorbing boundaries (perfectly matched layers, PML) are used to eliminate reflection. The axial symmetry of the system is used to minimize the calculation time and resources. The excitation source used is a point dipole positioned on top of the antennas, 1 nm above the apex and oriented parallel to the longitudinal axis. Figure 5a–g shows the simulation results—normalized electric field intensity—for the seven nanoantennas. We find good agreement between the calculated number of emitted lobes and the experimental data.

In Figure 6 we compare the measured polar emission profile and the numerical calculations. The blue curves show the measured emitted photon count from the nanoantennas at 650 nm wavelength and red ones show the numerical calculation of electric field intensity at the same wavelength. The measured and calculated values independently are normalized to their maximum value. The polar plot for measured data is obtained by cross-cutting the angle-resolved data along the radial axis. Both experiment and theory in Figure 6 show the strong angular modulation of the emitted intensity, with the number of lobes corresponding for theory and experiment. The experimental angular profiles are not precisely reproduced. This mismatch is attributed to the experimental uncertainties of the measured and estimated parameters of the nanoantennas. The measured parameters are the antenna height and core and gold thickness. In addition to those parameters the refractive index of the deposited silica core is not accurately known.

From a geometrical point of view our pillar type nanoantennas, standing perpendicular to the gold surface, resemble ground plane antennas working in the RF regime. Standing perpendicular on top of a conducting plane has a role of bringing out a mirror image on the other side. Antennas working in the RF regime are assumed to be a perfect metal that reflects the electromagnetic field without penetration unlike their dispersive plasmonic counterparts.[26,27] To illustrate the similarity and difference between the conventional ground plane (RF) antennas and our core–shell nanoantennas we perform a simulation such that the dimensions of the nanoantennas and the measured wavelength are scaled up by 5 orders of magnitude in order to reach the RF regime. The ratio between the antenna length and the wavelength (L/λ) is kept the same as that of nanoantennas. By keeping the length to wavelength ratio the same we compare the effective length of the nanoantenna and RF antenna in terms of emitted number of lobes. The simulated RF antennas consist of a metallic ground plane, coaxial feed, and a cylindrical antenna body. The entire system is inside a similar hemispherical simulation box as described above. The polar plot in Figure 7 shows the comparison between the longest nanoantenna and its simulated RF antenna counterpart normalized to the measured data. The comparison is established in terms of the emitted number of lobes and the directivity. The blue curve corresponds to the measured photon emission rate of the longest (2100 nm) nanoantenna at 650 nm and the red curve corresponds to the electromagnetic emission at a wavelength of 6.5 cm of the 21 cm long RF antenna. Thus the lengths of both antenna $L = 3.23\lambda$) is kept the same for both antennas. From the figure it is clear that the optical nanoantenna radiates six lobes (at the wavelength of 650 nm), whereas the RF antenna (at the wavelength of 6.5 cm) radiates four lobes. The effective length of our nanoantenna increases by a factor of 1.5 when going from RF to the optical regime.

The measurements and calculations—presented in Figure 3 and Figure 5, respectively—show that the vertical dipole excites the radially symmetric mode along the nanoantenna. As a result of this agreement between the measurement and simulation on the radially excited modes, we calculate the effective refractive index (n_{eff}) in order to clarify the role of the SPP on the nanoantennas optical properties. The mode solver feature of COMSOL is applied to an infinitely long nanorod composed of silica core and gold cladding. n_{eff} is calculated as a function of both Au shell thickness (which varies from 15 to 30 nm) and silica radius (50–75 nm) at 650 nm wavelength (see Figure 8). The inset shows the plasmonic radially symmetric mode[28] confined to the surface of the nanoantenna. The effective mode index,

$$n_{\mathrm{eff}} = \frac{k_{\mathrm{SPP}}}{k_{\mathrm{RF}}} \qquad (1)$$

determines by how much the effective length of a nanoantenna increases when its geometrical length increases.[29] The result of the effective mode index

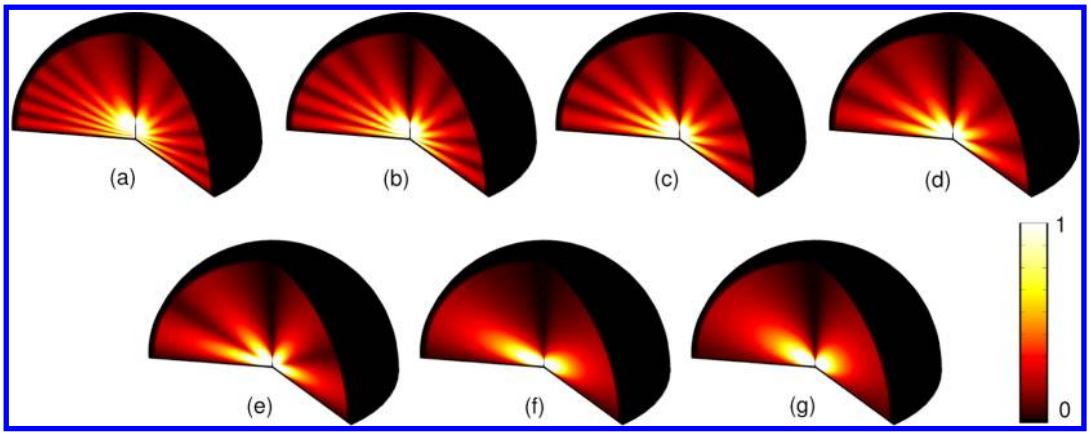

Figure 5. Finite element calculations of the nanoantennas. The structure is inside the hemisphere simulation box. The walls of the hemisphere are totally absorbent (perfectly matched layer, PML) to eliminate interference due to the reflection from the walls. Antennas were excited by a point like electric dipole positioned on the top of the each rod. The dipole is oriented parallel to the nanoantennas' longitudinal axis. From (a) to (g) it is shown that number of lobes are directly related to the length of the antennas. Color scale corresponds to the normalized E field amplitude.

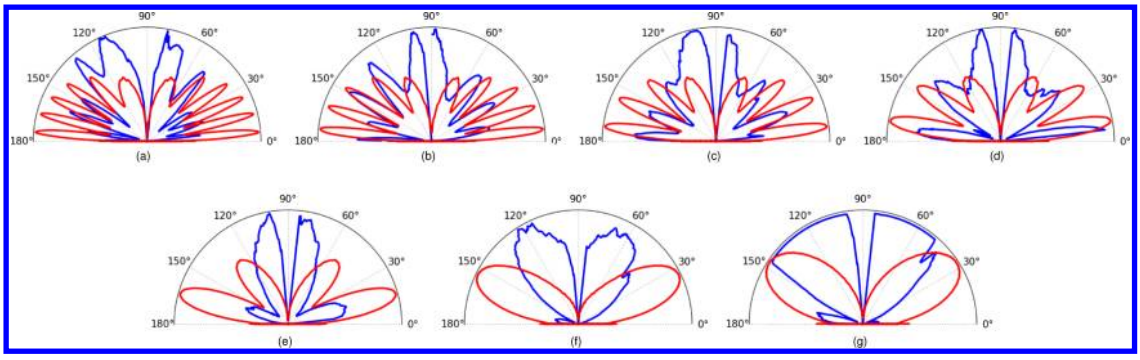

Figure 6. Comparison of the measured angle-resolved emission (blue line) and numerical calculations of the E field intensity (red line). Each data set is normalized where the highest data point, that is, maximum value, on every polar plot corresponds to unity.

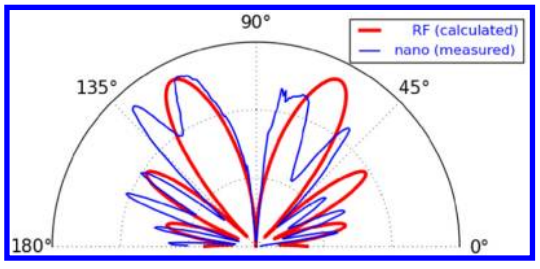

Figure 7. The number of emitted lobes of the longest nanoantenna is compared with its RF counterpart. The blue and red lines are associated with nano- and RF antennas, respectively. The length of the antennas is 3.23λ where λ is equal to 650 nm and 6.5 cm for nano and RF antenna, respectively.

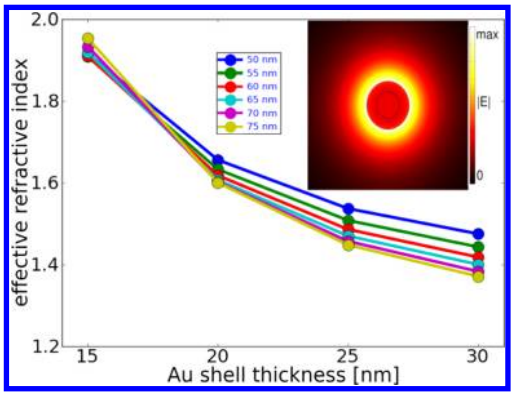

Figure 8. Calculated effective refractive index calculations for core–shell type nanoantennas as a function of gold shell thickness for different total rod radius (from 50 to 75 nm). The *E* field intensity is shown as an inset for the antenna with 65 nm radius and 30 nm cladding thickness. n_{eff} is highly dispersive in terms of gold shell thickness and total rod radius.

simulation is depicted in Figure 8 and clearly shows that the effective refractive index of the core–shell nanoantenna highly depends on both the Au shell thickness and the silica core radius. n_{eff} increases when either shell thickness or silica core radius are decreased. The maximum n_{eff} is observed for the thinest Au shell (15 nm) and core radius (50 nm). The effective index calculation now explains why the effective length of the RF and our nanoantenna appears longer than that of optical nanoantenna. Indeed, for the 50 nm core radius antennas with a 30 nm thick gold shell, the effective refractive index is 1.47 (blue curve in Figure 8). The plasmonic behavior and the dispersive refractive index thus strongly affect the radiation profile.

CONCLUSION

We have successfully fabricated high aspect ratio silica−gold nanoantennas by using electron-beam induced deposition (EBID) of silica combined with gold sputtering. The radiation profiles of the nanoantennas, with lengths in the range of 300−2100 nm, is measured using angle-resolved cathodoluminescence spectroscopy. The three-dimensional emission patterns and the numerical calculations reveal that the nanoantennas act as ground plane monopole antennas with an effective mode index that is determined by the silica core radius and gold cladding thickness. The large tunability of the antenna geometry with EBID in combination with the strongly dispersive plasmon propagation along the antennas enables the fabrication of optical antennas with tailored angular radiation profiles.[30−32]

METHOD

The silica core of the nanoantennas is fabricated by electron beam induced deposition (EBID).[33,34] Subsequently, a conformal gold shell is sputtered onto the silica pillars and the gold substrate. A Helios NanoLab 600 Dual Beam system equipped with a gas injection system (GIS) is used for the fabrication of the silica core. During the EBID process a gaseous precursor molecule is delivered within ~200 μm above the surface by means of a gas injection needle inside the vacuum chamber. Precursor molecules are adsorbed by the surface and secondary electrons (SE) scattered from the substrate dissociate these adsorbed molecules. The reaction ends with intended solid deposition on the substrate and a vapor byproduct that is removed from the chamber by the pumping system.

To deposit silica we use tetraethyl orthosilicate (TEOS, $Si(OC_2H_5)_4$) and water vapor as precursors. The TEOS and water are delivered to the vacuum chamber with the GIS and converted to solid silica deposition and ethanol byproduct according to the following reaction: $Si(OC_2H_5)_4 + 2H_2O \rightarrow SiO_2 + 4C_2H_5OH$. During the deposition process the chamber pressure is $\sim 3 \times 10^{-5}$ millibar. The electron beam current and acceleration energy were 0.17 nA and 5 kV, respectively. Following the silica deposition, 30 nm of gold is sputtered to the whole sample.

The silica cores of the nanoantennas are grown on a substrate which is composed of a 30 nm gold layer coating a silicon wafer. The EBID of the silica cores proceeds as follows. Each nanoantenna core is composed of a series of disks with each disk deposited on top of each of the last. The height of the nanoantenna is controlled by altering the number of disks deposited. Each disk is deposited by moving the focused electron beam around a series concentric circular tracks. The dwell time of the electron beam on each point of the track is 200 ns, and the total dose delivered (for the tallest structures) is 750 nC/μm^2.

Conflict of Interest: The authors declare no competing financial interest.

Acknowledgment. The authors thank Hans Zeijlemaker for technical support. This work is part of the research program of the Stichting voor Fundamenteel Onderzoek der Materie (FOM), cofinanced by FEI Company. The work is also supported by the research program NanonextNL, funded by the Dutch ministry of economic affairs.

REFERENCES AND NOTES

1. Tesla, N. Method of and appartus for controlling mechanism of moving vessels or vehicles. U. S. Patent 1898, 613809.
2. Novotny, L.; van Hulst, N. Antennas for Light. *Nat. Photon.* **2011**, *5*, 83–90.
3. Giannini, V.; Fernandez-Dominguez, A. I.; Heck, S. C.; Maier, S. A. Plasmonic Nanoantennas: Fundamentals and Their Use in Controlling the Radiative Properties of Nanoemitters. *Chem. Rev.* **2011**, *111*, 3888–3912.
4. Balanis, A. *Antenna Theory Analysis and Design*, 3rd ed.; Wiley-Interscience: NJ, 2005.
5. David, C.; García de Abajo, F. J. Spatial Nonlocality in the Optical Response of Metal Nanoparticles. *J. Phys. Chem. C* **2011**, *115*, 19470–19475.
6. Hentschel, M.; Schoeferling, M.; Weiss, T.; Liu, N.; Giessen, H. Three-Dimensional Chiral Plasmonic Oligomers. *Nano Lett.* **2012**, *12*, 2542–2547.
7. Curto, A. G.; Volpe, G.; Taminiau, T. H.; Kreuzer, M. P.; Quidant, R.; van Hulst, N. F. Unidirectional Emission of a Quantum Dot Coupled to a Nanoantenna. *Science* **2010**, *329*, 930–933.
8. Deutsch, B.; Hillenbrand, R.; Novotny, L. Visualizing the Optical Interaction Tensor of a Gold Nanoparticle Pair. *Nano Lett.* **2010**, *10*, 652–656.
9. Djaker, N.; Hostein, R.; Devaux, E.; Ebbesen, T. W.; Rigneault, H.; Wenger, J. Surface Enhanced Raman Scattering on a Single Nanometric Aperture. *J. Phys. Chem. C* **2010**, *114*, 16250–16256.
10. Atwater, H. A.; Polman, A. Plasmonics or Improved Photovoltaic Devices. *Nat. Mater.* **2010**, *9*, 205–213.
11. Thongrattanasiri, S.; Koppens, F. H. L.; García de Abajo, F. J. Complete Optical Absorption in Periodically Patterned Graphene. *Phys. Rev. Lett.* **2012**, *108*, 047401.
12. Jun, Y. C.; Huang, K. C.; Brongersma, M. L. Plasmonic Beaming and Active Control over Fluorescent Emission. *Nat. Commun.* **2011**, *2*, 283.
13. Muskens, O. L.; Giannini, V.; Sànchez-Gil, J. A.; Gòmez Rivas, J. Strong Enhancement of the Radiative Decay Rate of Emitters by Single Plasmonic Nanoantennas. *Nano Lett.* **2007**, *7*, 2871–2875.
14. Schnell, M.; Garcia-Etxarri, A.; Huber, A. J.; Crozier, K.; Aizpurua, J.; Hillenbrand, R. Controlling the Near-Field Oscillations of Loaded Plasmonic Nanoantennas. *Nat. Photon.* **2009**, *3*, 287–291.
15. Mühlschlegel, P.; Eisler, H.-J.; Martin, O. J. F.; Hecht, B.; Pohl, D. W. Resonant Optical Antennas. *Science* **2005**, *308*, 1607–1609.
16. Kim, S.; Jin, J.; Kim, Y.; Park, I.; Kim, Y.; Kim, S. High-Harmonic Generation by Resonant Plasmon Field Enhancement. *Nature* **2008**, *453*, 757–760.
17. Boltasseva, A. Plasmonic Components Fabrication *via* Nanoimprint. *J. Opt. A* **2009**, *11*, 114001.
18. Dregely, D.; Taubert, R.; Dorfmuller, J.; Vogelgesang, R.; Kern, K.; Giessen, H. 3D optical Yagi Uda Nanoantenna Array. *Nat. Commun.* **2011**, *2*, 267.
19. Taminiau, T. H.; Moerland, R. J.; Segerink, B., Frans; Kuipers, L.; van Hulst, N. F. $\lambda/4$ Resonance of an Optical Monopole Antenna Probed by Single Molecule Flourescence. *Nano Lett.* **2007**, *7*, 28–33.
20. Lindquist, N. C.; Nagpal, P.; Lesuffleur, A.; Norris, D. J.; Oh, S. Three-Dimensional Plasmonic Nanofocusing. *Nano Lett.* **2009**, *10*, 1369–1373.
21. van Kouwen, L.; Botman, A.; Hagen, C. W. Focused Electron-Beam-Induced Deposition of 3 nm Dots in a Scanning Electron Microscope. *Nano Lett.* **2009**, *9*, 2149–2152.
22. Coenen, T.; Vesseur, E. J. R.; Polman, A. Angle-Resolved Cathodoluminescence Spectroscopy. *Appl. Phys. Lett.* **2011**, *99*, 143103.
23. Coenen, T.; Vesseur, E. J. R.; Polman, A.; Koenderink, A. F. Directional Emission from Plasmonic Yagi Uda Antennas Probed by Angle-Resolved Cathodoluminescence Spectroscopy. *Nano Lett.* **2011**, *11*, 3779–3784.
24. COMSOL 4.2. http://www.comsol.com.

25. Palik, E. D. *Handbook of Optical Constants*; Academy Press: New York, 1985.
26. Novotny, L. Effective Wavelenth Scaling for Optical Antennas. *Phys. Rev. Lett.* **2007**, *98*, 266802.
27. Taminiau, T. H.; Stefani, F. D.; van Hulst, N. F. Optical Nanorod Antennas Modelled as Cavities for Dipolar Emitters: Evolution of Sub- and Super-radiant Modes. *Nano Lett.* **2011**, *11*, 1020–1024.
28. Sommerfeld, A. Uber die Fortpflanzung Elektrodynamischer Wellen Langs Eines Drahtes. *Ann. Phys. (Berlin)* **1899**, *303*, 233.
29. Cubukcu, E.; Capasso, F. Optical Nanorod Antennas as Dispersive One-Dimensional Fabry-Perot Resonators for Surface Plasmons. *Appl. Phys. Lett.* **2009**, *95*, 201101.
30. King, N. S.; Li, Y.; Ayala-Orozco, C.; Brannan, T.; Nordlander, P.; Halas, N. J. Angle- and Spectral-Dependent Light Scattering from Plasmonic Nanocups. *Nano Lett.* **2011**, *5*, 7254–7262.
31. Zhang, Y.; Barhoumi, A.; Lassiter, J. B.; Halas, N. J. Orientation-Preserving Transfer and Directional Light Scattering from Individual Light-Bending Nanoparticles. *Nano Lett.* **2011**, *11*, 1838–1844.
32. Alú, A.; Engheta, N. Tuning the Scattering Response of Optical Nanoantennas with Nanocircuit Loads. *Nat. Photon.* **2008**, *2*, 307–310.
33. van Dorp, W. F.; Hagen, C. W. A Critical Literature Review of Focused Electron Beam Induced Deposition. *J. Appl. Phys.* **2008**, *104*, 081301.
34. Randolph, S. J.; Fowlkes, J. D.; Rack, P. D. Focused, Nanoscale Electron-Beam-Induced Deposition and Etching. *Crit. Rev. Solid State Mater. Sci.* **2006**, *31*, 55–89.